

Refractive versus resonant diffraction scattering of loosely bound ${}^6\text{Li}$ nuclei

Florin Carstoiu¹ and Livius Trache^{1,2}¹National Institute for Physics and Nuclear Engineering “Horia Hulubei,” P.O. Box MG-6, 76900 Bucharest-Magurele, Romania²Cyclotron Institute, Texas A&M University, College Station, Texas 77843-3366, USA

(Received 18 December 2011; revised manuscript received 2 March 2012; published 4 May 2012)

We present a complete analysis of ${}^6\text{Li} + {}^{16}\text{O}$ elastic scattering at 4 and 5 MeV/nucleon. Using either traditional Woods-Saxon or a range of semimicroscopic folding form factors we find that the data require deep, highly transparent potentials. Physically relevant solutions are selected according to the dispersion relation. The intermediate angle structures and the oscillatory increase of the cross section at large angles are interpreted either as a pre-rainbow oscillation resulting from the interference of the barrier and internal barrier far-side scattering subamplitudes or, equally well, as a resonant diffraction arising from two Regge poles located in peripheral waves. Both semiclassical and Regge pole approaches allow a dynamical separation of the resonant component of the S matrix.

DOI: [10.1103/PhysRevC.85.054606](https://doi.org/10.1103/PhysRevC.85.054606)

PACS number(s): 25.70.Bc, 25.70.Ef, 24.10.Ht

I. INTRODUCTION

The study of nucleus-nucleus elastic scattering has a long history but remains of interest due to both successes and failures that mark it (see, for example, Refs. [1,2] and references therein). We are searching here for reliable ways to predict optical model potentials for reactions with radioactive nuclear beams (RNBs). In particular, our interest focuses on finding reliable descriptions for transfer and breakup reactions involving relatively light, loosely bound nuclei, which are used in indirect methods in nuclear astrophysics. A range of RNB studies were made at energies around 10 MeV/nucleon, where the reactions are peripheral, with the intent to obtain information about stellar reaction rates. These reactions use DWBA techniques to extract nuclear structure information. However, the well-known existence of many ambiguities in the optical model potentials (OMPs) extracted from elastic scattering can raise questions about the reliability and accuracy of these determinations. Experimental studies using RNBs have, heretofore, not been suitable for detailed elastic scattering analyses. The best information comes from studying the elastic scattering of stable loosely bound nuclei with similar mass. We chose here to study the elastic scattering of ${}^6\text{Li}$ at low energy, a fragile projectile (loosely bound), with a pronounced cluster structure and with low Z that can, therefore, exhibit a range of phenomena, involving absorption, resonant diffraction, and refraction, mostly of nuclear nature. We continue here the efforts started in Refs. [3,4] to find a way to predict optical potentials for scattering involving radioactive nuclei, or, at least, to have a good starting point for obtaining them, after which they are only fine tuned using the available, lower quality, scattering data with RNBs. We consider that in order to reach this goal it is important to study and understand in detail the mechanisms involved in the scattering of nuclei with some similarities. This may help to eliminate some of the ambiguities and interpretations that are known to plague the description of elastic scattering with optical potentials. This goal can be achieved only with very good data, covering well a wide angular range, and at different bombarding energies.

Works by Ogloblin *et al.* [5] and by Szilner *et al.* [6] have established that elastic scattering of light, tightly bound

heavy-ion systems such as ${}^{16}\text{O} + {}^{12}\text{C}$ and ${}^{16}\text{O} + {}^{16}\text{O}$ show sufficient transparency for the cross section to be dominated by the far-side scattering. Intermediate-angle structures appearing in the elastic scattering distributions at angles beyond the Fraunhofer diffractive region have been identified as Airy minima of a nuclear rainbow, i.e., destructive interference between two far-side trajectories which sample the interior of the potential. A number of high-order Airy minima have been identified by observing that such structures are largely insensitive to an artificial reduction of the absorption in the optical potential, and therefore they appear as a manifestation of the refractive power of the nuclear potential. While at high energy [7] this picture was well substantiated by a semiclassical nonuniform decomposition of the scattering function [8], at lower energies the situation is more difficult to understand. It has been shown by Anni [9] that such structures could be explained by the interference of two amplitudes appearing in different terms of a multireflection uniform series expansion of the scattering amplitude and therefore the interpretation using rainbow terminology is not appropriate.

For loosely bound nuclei at low energy the situation is even more intricate.

The corresponding components in the optical potential are expected to be more diffuse as compared to normal nuclei, leading to a competition between the increased refractive power of the real potential and the increased absorption at the nuclear surface. The small separation energy implies also that the dynamic polarization potential (DPP) [10] arising from the coupling to breakup states may be strong and have a complicated energy and radial dependence. Thus the DPP cannot be treated as a small perturbation for loosely bound nuclei and the usual phenomenological procedure in renormalizing the folding potential form factor may be questioned. It has been estimated that the DPP is strongly repulsive at the nuclear surface in the case of ${}^6\text{Li}$ [11]. This prompted Mahaux, Ngo, and Satchler [12] to conjecture that for loosely bound nuclei the barrier anomaly may be absent due to the cancellation between the repulsive (DPP) and attractive (dispersive) components of the optical potential.

Folding model analysis using the complex, density- and energy-dependent NN interaction of Jeukenne, Lejeune, and Mahaux (JLM) [13], as well as other G -matrix effective interactions, where corrections due to the strong DPP have been included, confirmed that the elastic distribution could be described using deep and extremely transparent potentials. The intermediate-angle structures have been discussed using the semiclassical uniform approximation for the scattering function of Brink and Takigawa [14]. We explain the intermediate-angle structure as a coherent interference effect of two subamplitudes corresponding to trajectories reflected at the barrier and interfering with trajectories which sample the nuclear interior. Thus, this refractive effect appears as a signature of a highly transparent interaction potential. A completely different picture emerges using a phenomenological Regge pole analysis [15], pointing to a resonant effect present in surface waves.

In this paper we present an analysis of elastic scattering of ${}^6\text{Li}$ on ${}^{16}\text{O}$ at 4 and 5 MeV/nucleon. Accurate angular distribution has been measured over an almost complete angular range [16,17]. This angular distribution displays a complex structure at intermediate and large angles, pointing to strong refractive effects.

The paper is structured in the following way: after this introduction, the analysis of the elastic scattering data using phenomenological and microscopic optical model potentials is discussed in Sec. II. In Sec. III we present a discussion of the decomposition of the far-side scattering amplitude into barrier and internal barrier components responsible for the exotic structure at intermediate angles. Finally, we perform a Regge pole analysis in Sec. IV and conclude our work in Sec. V.

II. OPTICAL-MODEL ANALYSIS

A. Woods-Saxon form factors

The measured elastic scattering data at $E_{\text{lab}} = 25.7$ MeV and 29.8 MeV [16,17], shown in Fig. 1 as the ratio to the Rutherford cross section, covers a large angular range. These data show complex forms with characteristic rapid oscillations at small angles followed by a marked change in shape at intermediate angles: a bump develops at $\theta \approx 100^\circ$ (25.7 MeV) or a shallow minimum (29.8 MeV), which is followed by a significant increase of the cross section at larger angles, reminding the well-known anomalous large-angle scattering (ALAS; see a review in [18]). Assuming pure Fraunhofer scattering at forward angles, we extract a grazing angular momentum, $l_g \approx 12$, from the angular spacing $\Delta\theta = \pi/(l_g + 1/2)$.

The data are analyzed using optical potentials with conventional Woods-Saxon (WS) form factors for the nuclear term, supplemented with a Coulomb potential generated by a uniform charge distribution with a reduced radius fixed to $r_c = 1$ fm. No preference has been found for volume- or surface-localized absorption and throughout the paper only volume absorption is considered. In the absence of any spin-dependent observables, spin-orbit or tensor interactions have been ignored. Ground-state reorientation couplings also have been neglected. The potential is defined by six parameters specifying the depth and geometry of the real and imaginary

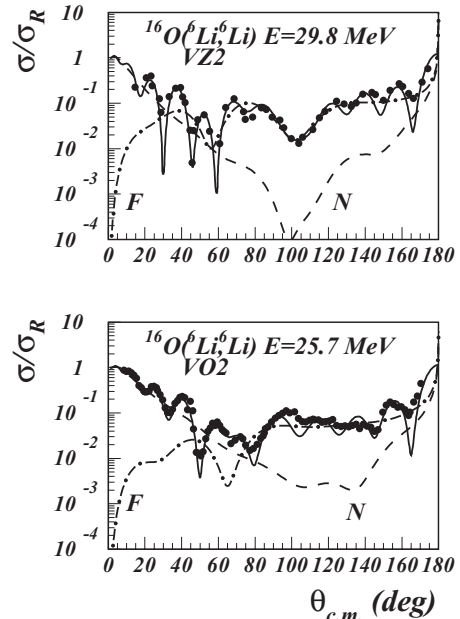


FIG. 1. Woods-Saxon optical model analysis (full lines) of elastic scattering data (points) at 4 and 5 MeV/nucleon (Table I). Far-side (dash-dotted line) and near-side (dash line) cross sections are also shown as a ratio to the Rutherford cross section.

terms, with the standard notation, the same as used in Ref. [3]. The number of data points, N , is quite large, and consequently the usual goodness-of-fit criteria (χ^2) normalized to N has been used.

The averaging associated with the finite experimental angular resolution mostly affects the depth of sharp minima. A few exploratory calculations showed that allowing the overall normalization to vary did not result in any qualitative changes and did not indicate that any renormalization of the data by more than a few percent would be preferred. Optical parameter sets obtained in our previous paper [4] were used as starting values for the search procedure. Guided by these potentials and by our earlier analysis [3] a number of some 10^4 potentials with real volume integrals in the range $J_V = 200\text{--}600$ MeV fm³ have been generated, thus exploring the functional Woods-Saxon space in full detail. Local minima were identified and a complete search on all six parameters determined the best-fit potentials. The complex structure at intermediate angles and the increase of the cross section at large angles could be described only with deep potentials with real volume integrals (per pairs of interacting nucleons) exceeding a critical value $J_{V \text{ crit}} \approx 240$ MeV fm³. We did not find any acceptable solution with $J_V < 200$ MeV fm³ (see Fig. 2). There is a consistent preference for potentials with very weak imaginary parts, with values of W around 5–7 MeV. We systematically find $r_V < r_W$ and large diffuseness parameters $a_V \simeq 0.9$ fm, in agreement with theoretical expectations for loosely bound nuclei [19,20]. A grid search procedure on the real depth of the potential allowed us to identify discrete ambiguities. The best solutions which match quite well the dispersion relations (see below) are given in Table I. For each discrete solution we found an almost constant imaginary

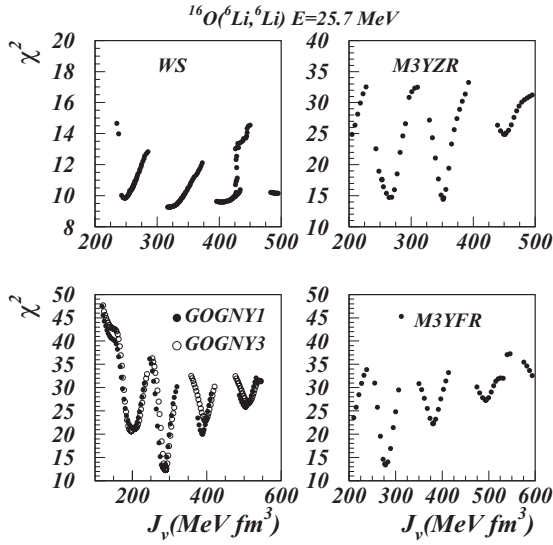


FIG. 2. Discrete ambiguities obtained from a grid search on the real volume integral, using Woods-Saxon (WS) and double folding form factors in the optical model. There are no acceptable solutions with $J_V < 200 \text{ MeV fm}^3$. Best solutions are tabulated in Table I.

volume integral. As a consequence, the total reaction cross section seems to be a well-determined observable. Gridding on other WS parameters revealed a continuous ambiguity of the form $J_V R_V \approx \text{const.}$, where R_V is the rms radius of the potential. The larger the volume integral, the smaller the radius that is required to fit the data. This is a clear manifestation of a complicated radial dependence of the DPP, which may lead to radii much smaller than the minimal value implied by the folding model (e.g., $R_F^2 = R_1^2 + R_2^2$, for a zero-range NN effective interaction). However, for each discrete family

rather precise values of the rms radii were required to fit both forward- and intermediate-angle cross sections.

As mentioned already, it was shown in Refs. [5–7] that the elastic scattering of light heavy ion systems such as $^{16}\text{O} + ^{12}\text{C}$ and $^{16}\text{O} + ^{16}\text{O}$ shows sufficient transparency for the cross section to be dominated by far-side scattering. Structures appearing in the elastic scattering angular distributions at intermediate angles have been identified as Airy minima of a nuclear rainbow, due to destructive interference between two far-side trajectories which sample the interior of the potential. At 4 MeV/nucleon the ^6Li scattering data show rapid, diffractive Fraunhofer oscillations at forward angles due to the strong near-far amplitude interference (Fig. 1). At $\theta \approx 40^\circ$ the far-side and near-side components of the scattering amplitude are almost equal, producing the first Fraunhofer deep minimum. Beyond this “crossover” the near-side amplitude makes a negligible contribution and the cross section is dominated by the far-side component. There is no dark-side exponential decay of the far-side component. The deep minimum seen at $\theta \approx 60^\circ$ in the far-side component is stable against the strength of the absorption and may be interpreted as a primary Airy minimum of a nuclear rainbow. It is followed by a broad Airy maximum and a structureless increase of the far-side cross section at large angles. Low-amplitude oscillation of the elastic cross section at intermediate and large angles are due to far-side/near side interference. The total cross section reaches a maximum near $\theta = 180^\circ$ where both components became again equal. Clearly, far-side dominance may be interpreted as a possible manifestation of refractive effects. However, this simple dominance does not explain, by itself, the structure of the far-side component. In fact, the above picture has already been challenged by Anni [9] and by Michel *et al.* [21] for the simple reason that the far-side amplitude has never been decomposed into subamplitudes which would explain the interference. We shall return to this topic in Sec. III. For the

TABLE I. Best-fit Woods-Saxon and folding potential parameters for $^6\text{Li} + ^{16}\text{O}$ which match the dispersion relation. The second header line denotes parameters for folding potentials. Reduced radii are defined in the heavy-ion convention. All lengths are given in femtometers, depths in MeV, cross sections in millibarns, and volume integrals in MeV fm^3 . R_V and R_W are the rms radii of the real and imaginary potentials, respectively. The normalized χ^2 values are calculated by assuming a uniform 10% error.

E_{lab}	Potential	V_0	W_0	r_V	r_W	a_V	a_W	χ^2	σ_R	J_V	R_V	J_W	R_W
		N_V	N_W	t_V	t_W								
25.7	VO1	162.21	5.018	0.529	1.469	0.993	0.654	9.81	1434	248	4.087	63	5.502
	VO2	224.00	5.988	0.541	1.415	0.911	0.687	9.27	1430	318	3.839	68	5.397
	M3YZR	0.737	0.139	0.090	2.799			14.4	1499	352	3.908	62	5.208
	M3YFR	0.492	0.105	0.364	2.904			13.3	1532	279	4.058	59	5.387
	GOGNY1	0.426	0.092	0.383	2.944			12.6	1540	284	4.072	60	5.427
	GOGNY3	0.520	0.114	0.083	2.844			12.3	1534	289	4.100	61	5.386
	JLM1	0.543	0.428	0.646	2.795			11.5	1513	354	3.879	64	5.327
JLM3	0.588	0.532	0.733	2.763			11.6	1509	350	3.871	63	5.296	
29.8	VZ2	237.51	7.268	0.506	1.338	1.006	0.607	7.35	1369	344	4.098	68	5.029
	M3YZR	0.730	0.148	0.105	2.977			10.9	1578	345	3.909	66	5.356
	M3YFR	0.705	0.132	0.385	2.849			11.6	1543	363	3.943	67	5.252
	GOGNY1	0.610	0.109	0.279	2.634			12.8	1505	378	3.974	67	5.114
	GOGNY3	0.750	0.139	0.098	2.549			13.0	1501	386	4.000	68	5.080
	JLM1	0.555	0.439	0.824	2.638			11.4	1518	359	3.930	67	5.200
	JLM3	0.595	0.548	0.865	2.711			10.9	1532	352	3.912	66	5.249

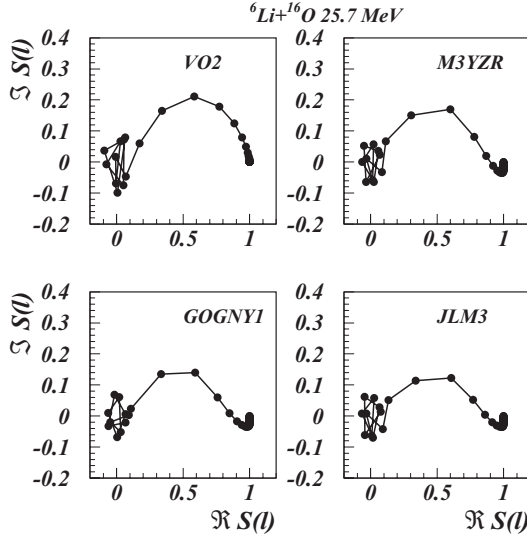


FIG. 3. Argand diagrams for the WS and folding S matrix. Optical potentials are from Table I. For low angular momentum $l < 10$, the trajectory for the S matrix rotates clockwise several times around the origin, suggesting the presence of several Regge poles.

moment we adopt the interpretation of Michel *et al.* [21] and denote the complex structure at intermediate angles in the data as pre-rainbow oscillations. A model-independent analysis in which the diagonal S -matrix elements are extracted directly from the data through a complex phase shift analysis confirms that the Airy oscillation at $\theta \approx 60^\circ$ is a real effect. Further information can be obtained by looking at the Argand diagrams displayed in Fig. 3. It demonstrates that the potentials given in Table I are fully equivalent since the Argand patterns are almost identical for all potentials. This means that the Drisko ambiguity [22], $\delta_l \rightarrow \delta_l + n\pi$, holds not only for low angular momenta but for all momenta when going from one potential to another. Furthermore, for low angular momentum $l < 10$, the trajectory for the S matrix rotates clockwise several times around the origin, suggesting the presence of several Regge poles. We will return to this effect in the following sections.

B. Folding model analysis

In this section we discuss the ability of the folding model to describe the pre-rainbow oscillation seen in our data.

We start with a quite simple model in which the form factors of the OMP are given by the double folding integral

$$V_{\text{fold}}(R) = \int d\vec{r}_1 d\vec{r}_2 \rho_1(r_1) \rho_2(r_2) v_{M3Y}(s), \quad (1)$$

where v_{M3Y} is the M3Y parametrization of the G matrix obtained from the Paris NN interaction [23], and $\vec{s} = \vec{r}_1 + \vec{R} - \vec{r}_2$ is the NN separation distance. In the simplest version of this model, dubbed here as M3YZR, the knock-on exchange component is simulated by a zero-range potential with a slightly energy-dependent strength,

$$J_0(E) = -276(1 - 0.005E/A). \quad (2)$$

Then the OMP is given by

$$U(R) = N_V V(R, t_V) + N_W W(R, t_W), \quad (3)$$

where $N_{V,W}$ are normalization constants and $t_{V,W}$ are range parameters of a smearing function

$$g(\vec{s}) = \frac{1}{t^3 \pi^{3/2}} \exp(-s^2/t^2). \quad (4)$$

With this function, the form factors of the OMP are given by

$$V(R, t_V) = \int d\vec{R}' V_{\text{fold}}(R') g(\vec{R} - \vec{R}') \quad (5)$$

and similarly for $W(R, t_W)$. Note that the normalized function g converges to a δ function in the limit $t \rightarrow 0$. The rms radius of the OMP form factor is given by

$$\langle r^2 \rangle_V = \langle r^2 \rangle_{\rho_1} + \langle r^2 \rangle_{\rho_2} + \langle r^2 \rangle_v + (3/2)t^2. \quad (6)$$

Thus the volume integral of the form factor is controlled by the parameters $N_{V,W}$. Note that the normalization in Eq. (4) ensures that only the rms radius of the bare folding potential is changed by the transformation of Eq. (5). Based on Eq. (6) one may estimate in an average way the importance of the dynamic polarization potential and finite-range effects. Throughout this paper we use single-particle densities obtained from a spherical Hartree-Fock (HF) calculation based on the density functional of Beiner and Lombard [24]. The obtained rms charge radii are $\langle r^2 \rangle_{6\text{Li}}^{1/2} = 2.33$ fm and $\langle r^2 \rangle_{16\text{O}}^{1/2} = 2.71$, which should be compared with experimental values of 2.53 and 2.70 fm, respectively [25]. A grid search on the real volume integral reveals the same ambiguity obtained with the WS form factors (see Fig. 2 and Table I). The best solutions are displayed in Fig. 4. The real volume integrals match quite well solutions found with the WS parametrization. Again imaginary volume integrals are quite small, pointing to a large transparency of the potential. Correction due to the finite-range effects are quite large, of the order of $\Delta r \approx 0.4$ fm for the

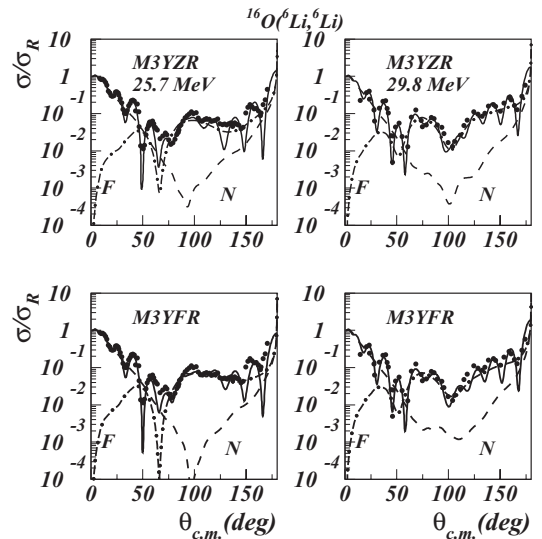


FIG. 4. Cross sections calculated with the zero-range (top) and finite-range (bottom) versions of the M3Y effective interaction at 25.7 MeV (left panels) and 29.8 MeV (right panels). Renormalization parameters and ranges are given in Table I.

real potential and much larger for the imaginary potential. Note that the minimum rms radius implied by Eq. (6) is 3.57 fm. Far-side/near-side decomposition of the scattering amplitude reveals the same features: a minimum in the far-side component develops at $\theta = 65^\circ$, which becomes deeper with the increased real volume integral of the interaction.

A more elaborate calculation leads to a nonlocal knock-on exchange kernel,

$$U_{ex}(\vec{R}^+, \vec{R}^-) = \mu^3 v_{ex}(\mu R^-) \int d\vec{X}_1 \rho_1(X_1) \hat{j}_1 \left[k_{f1}(X_1) \frac{(A_1 - 1)A_2}{A_1 + A_2} R^- \right] \times \rho_2 \left[|\vec{R}^+ - \vec{X}_1| \right] \hat{j}_1(k_{f2}(|\vec{R}^+ - \vec{X}_1|) \frac{(A_2 - 1)A_1}{A_1 + A_2} R^-), \quad (7)$$

where $A_{1,2}$ are mass numbers, μ is the reduced mass of the system, $k_{f1,2}$ are Fermi momenta, $R^{+,-}$ are the usual nonlocal coordinates, and v_{ex} is the exchange component of the interaction including the long-range one-pion exchange potential (OPEP) tail. In the lowest order of the Perey-Saxon approximation, the local equivalent of the nonlocal kernel is obtained by solving the nonlinear equation

$$U_L(R) = 4\pi \int d\vec{r}_1 d\vec{r}_2 \rho_1(r_1) \rho_2(r_2) \times \int s^2 ds v_{ex}(s) \hat{j}_1(k_{f1}(r_1) \beta_1 s) \hat{j}_1(k_{f2}(r_1) \beta_2 s) \times j_0 \left(\frac{1}{\mu} K(R) s \right) \delta(\vec{r}_2 - \vec{r}_1 + \vec{R}). \quad (8)$$

Here $\beta_i = (A_i - 1)/A_i$ are recoil corrections and $\hat{j}_1(x) = 3j_1(x)/x$ and $j_{0,1}$ are spherical Bessel functions. Local Fermi momenta k_f are evaluated in an extended Thomas-Fermi approximation [26]. The local momentum for the relative motion is given by

$$K^2(R) = \frac{2\mu}{\hbar^2} [E_{c.m.} - U_D(R) - U_L(R)], \quad (9)$$

where U_D is the total direct component of the potential including the Coulomb term. In Eq. (9) we assumed a purely real local momentum of the relative motion since the absorptive component of the OMP is small compared with the real part. The effective-mass correction [27], $\frac{\mu^*}{\mu} = 1 - \frac{\partial U}{\partial E}$, is of the order of a few percent for this system and is absorbed in the renormalization parameter N_W . Some tens of iterations are needed to solve Eq. (8) in order to obtain a precision of 10^{-7} in the entire radial range. Calculations with the finite-range model are dubbed M3YFR. As in the case of other interactions it is possible to find several solutions. However, a careful calculation reveals that in fact there is a *unique* solution with $J_V = 280 \text{ MeV fm}^3$ (Fig. 2). At 29.8 MeV we found a unique solution at about $J_V = 350 \text{ MeV fm}^3$. Thus the more careful calculation of the knock-on exchange component changes completely the volume integral and the rms radius of the real component such that a unique solution survives in the range $J_V = 250\text{--}350 \text{ MeV fm}^3$.

At this point we want to make a comment on the effect of coupling with the breakup states. Sakuragi [11] performed a

continuum discretized coupled channels (CDCC) calculation of ${}^6\text{Li}$ scattering over a large range of incident energies and target mass. He found that coupling with α - d breakup states brings a repulsive DPP in the nuclear surface in such a way that reasonable fits can be obtained by fixing the normalization constant $N_V = 1$ and $N_W = 0.4\text{--}0.7$ when using the M3Y effective interaction supplemented by a pseudo zero-range knock-on potential as we did in our model M3YZR. First, he assumes implicitly that M3Y is a perfect interaction and the renormalization N_V should be exactly one. This is not the case for several reasons. The absence of any explicit density dependence and of three-body effects leads to a collapse of the equation of state of nuclear matter at least at the HF level. The pseudo potential used for the knock-on exchange is a poor approximation. The odd components (SO and TO) of the interaction are largely ambiguous. We have seen that in a single-channel calculation there are discrete ambiguities with real volume integrals $J_V = 200\text{--}350 \text{ MeV fm}^3$. The bare (un-normalized) potential has a volume integral of 425 MeV fm^3 and an rms radius of 3.86 fm. This means that the DPP coming from coupling to breakup should correct simultaneously the volume integral by $\Delta J_V = 225, 165, \text{ and } 80 \text{ MeV fm}^3$ and for $\Delta R_V = 0.1\text{--}0.2 \text{ fm}$, which is evidently impossible. Furthermore, in line with our previous analyses [3,4] we found systematically $\Delta R = R_W - R_V \approx 1.4 \text{ fm}$ and therefore it is a bad approximation to use the same geometry for real and absorptive components of the OMP.

Is this unique solution an accidental feature of the M3YFR model? In a recent paper [28] we successfully described the hindrance in the sub-barrier fusion of ${}^{48}\text{Ca}$ with several targets using optical potentials generated with two parametrizations of the Gogny effective interaction. By neglecting the spin-orbit component, the Gogny NN interaction can be expressed as a sum of a central, finite-range term and a zero-range density-dependent term,

$$v(\vec{r}_{12}) = \sum_{i=1}^2 (W_i + B_i P_\sigma - H_i P_\tau - M_i P_\sigma P_\tau) e^{-\frac{r_{12}^2}{\mu_i^2}} + t_3 (1 + P_\sigma) \rho^\alpha(\vec{R}_{12}) \delta(\vec{r}_{12}), \quad (10)$$

where $\vec{r}_{12} = \vec{r}_1 - \vec{r}_2$, $\vec{R}_{12} = (\vec{r}_1 + \vec{r}_2)/2$, and standard notation has been used for parameter strengths and spin-isospin exchange operators. The strengths and the ranges are taken from [29]. The interest in this interaction resides in its excellent description (at the HF level) of the saturation properties of nuclear matter in line with modern estimation from the isoscalar giant monopole [30] or dipole resonance [31] studies. Antisymmetrization of the density-dependent term is trivial, so that the sum of direct and exchange terms reads

$$v_D^\rho(r_{12}) + v_{ex}^\rho(r_{12}) = \frac{3t_3}{4} \rho^\alpha \delta(\vec{r}_{12}). \quad (11)$$

The local equivalent of the finite-range knock-on exchange is calculated with Eq. (8). Two approximations were used for the overlap density,

$$\rho = [\rho_1(r_1) \rho_2(r_2)]^{1/2} \quad (12)$$

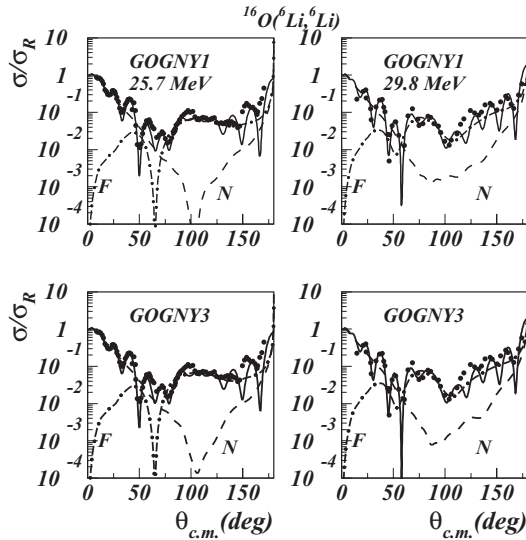


FIG. 5. Cross sections calculated with the D1 parametrization of the Gogny effective interaction. The curves in the top and bottom panels are calculated using Eqs. (12) and (13), respectively, for the overlap density. Renormalization parameters and ranges are given in Table I.

and

$$\rho = \frac{1}{2}[\rho_1(r_1) + \rho_2(r_2)]. \quad (13)$$

The first approximation, Eq. (12), has the merit that the overlap density goes to zero when one of the interacting nucleons is far from the bulk. The calculated OMPs are dubbed GOGNY1 and GOGNY3, respectively. Both definitions represent crude approximations of the overlap density but are widely used in the estimation of the density effects in the folding model. Several solutions have been found with this model, but in fact only one gives a fit comparable with the best solutions found with other form factors (Fig. 5). Estimation with the overlap density defined in Eqs. (12) or (13) do not make too much difference (Table I). Both approximations lead to the same volume integrals and rms radii.

We further examine the density-dependence effects by using the nuclear matter approach of Jeukenne, Lejeune and Mahaux (JLM) [13], which incorporates a complex, energy- and density-dependent parametrization of the NN effective interaction obtained in a Brueckner Hartree-Fock approximation from the Reid soft-core nucleon-nucleon potential. The systematic study [3] of the elastic scattering between p -shell nuclei at energies around 10 MeV/nucleon leads to the surprising result that, on average, the imaginary part of the folded JLM potential was perfectly adequate to describe such reactions and did not need any renormalization ($N_W = 1.00 \pm 0.09$), while the real component needed a strong renormalization, in line with other effective interactions used in folding models. We do not expect this property to be conserved at much lower energy (4–5 MeV/nucleon in this case).

There are no exchange components included in this model and, as a consequence, several discrete solutions are found. The

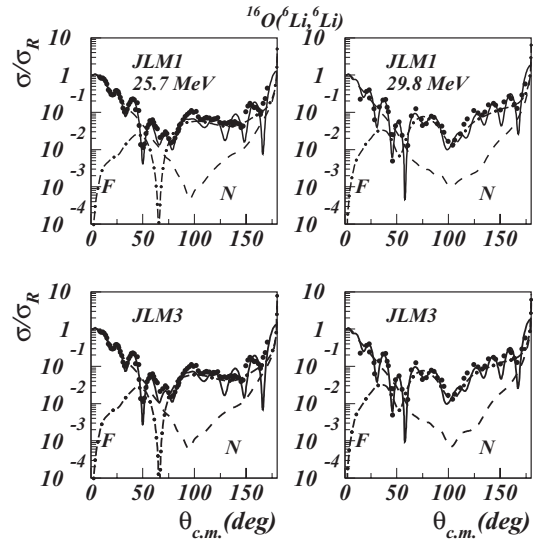


FIG. 6. Cross sections calculated with the G -matrix JLM effective interaction. The curves in the top and bottom panels are calculated using Eqs. (12) and (13), respectively, for the overlap density. Renormalization parameters and ranges are given in Table I.

best solutions obtained with Eqs. (12) and (13) are displayed in Fig. 6 and listed in Table I.

The JLM1 model provides a consistent description of the rainbow pattern in a large range of energies between 8 to 53 MeV/nucleon (see Fig. 7). At the lowest energy shown in Fig. 7, the broad hump at $\theta \approx 90^\circ$ is associated with a primary rainbow peak. As the energy increases, the primary rainbow moves forward and is followed by the exponential fall in the classically forbidden range.

In the remainder of this section we examine the dispersive properties of the optical potential for ${}^6\text{Li}$ scattering. The threshold anomaly which manifests itself as a sharp increase of the real optical potential for energies close to the Coulomb

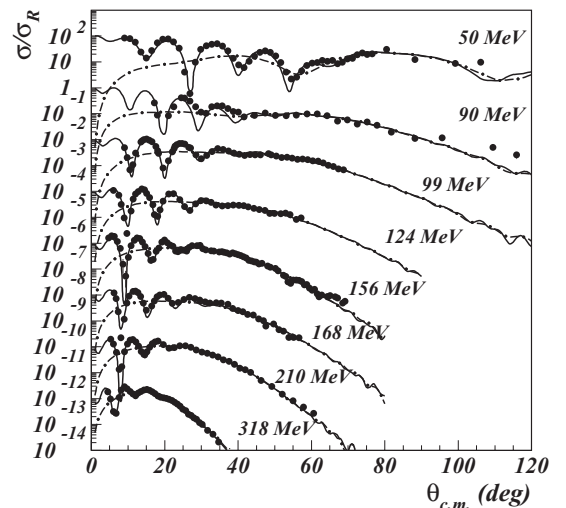


FIG. 7. Cross sections calculated with the JLM1 model for energies between 8 and 53 MeV/nucleon for the reaction ${}^6\text{Li} + {}^{12}\text{C}$. The far-side component is shown by dash-dotted lines. See also Ref. [4] for experimental data references.

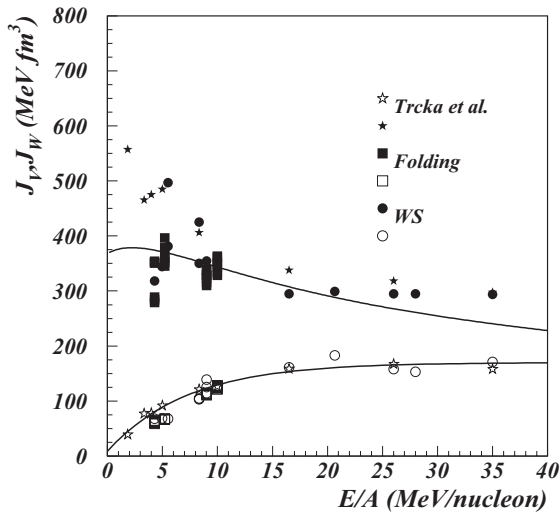


FIG. 8. Energy dependence of the real (solid points) and imaginary (open points) volume integrals obtained in the analyses with Woods-Saxon and folding optical potentials. The stars show the values obtained from the OM1 optical potential of Ref. [38]. Empirical values at high energy were taken from Ref. [4] for the reaction ${}^6\text{Li} + {}^{12,13}\text{C}$, by assuming that the mass dependence of the $J_{V,W}$ is weak. The curve for J_W is obtained from a best fit with Eq. (16) while the curve for J_V is the result from the dispersion relation, normalized to the empirical value at 20 MeV/nucleon.

barrier has been explained by Nagarajan, Mahaux, and Satchler [32] as due to the opening of reaction channels with increasing energy. Later on it was conjectured by Mahaux *et al.* [12] that, for loosely bound nuclei, this anomaly may be absent. Recent studies of the threshold anomaly in ${}^6,7\text{Li}$ -induced reactions lead to contradictory conclusions: a cancellation between the attractive (dispersive) component and the repulsive dynamic polarization potential [33,34], dynamic polarization potentials of opposite sign for ${}^6,7\text{Li}$ [35], and breakup suppression in complete fusion above the barrier energies [36]. A recent study of the ${}^6\text{Li}$ interaction with heavy targets [37] showed that prompt breakup triggered by neutron-stripping is more likely than prompt breakup into projectile cluster constituents. Therefore, the energy dependence of the ${}^6,7\text{Li}$ optical potential is far from clear and the competition between dispersive (attractive) and coupling to continuum (repulsive) effects needs to be studied more carefully. The real and imaginary volume integrals for the optical potentials obtained in the previous sections are plotted in Fig. 8. Both Woods-Saxon and folding results have been included. These are supplemented with values derived from the smooth OM1 potential of Trcka *et al.* [38], from [4], and from an analysis of ${}^6\text{Li} + {}^{12}\text{C}$ at 24 and 30 MeV [16], under the assumption that the mass dependence of the normalized volume integrals $J_{V,W}$ is weak.

We assume that the local optical potential may be written as $V = V_0 + \Delta V(E)$, where V_0 is independent of energy and $\Delta V(E)$ is the energy-dependent DPP. We ignore the spurious energy dependence of V_0 arising from nonlocality which is expected to be weak for heavy ions. We use the dispersion relation connecting the imaginary and real volume integrals in

the subtracted form

$$J_{\Delta V, E_s}(E) = (E - E_s) \frac{\mathcal{P}}{\pi} \int \frac{J_W(E')}{(E' - E_s)(E' - E)} dE', \quad (14)$$

which determines $J_{\Delta V}$ up to a constant. Here E_s is a reference energy and \mathcal{P} is the principal value of the integral. In principle the evaluation of this equation requires the knowledge of J_W values at all energies. The above subtracted form takes advantage of the fact that the energy dependence of J_W far from saturation energy is not very important and the unknown contributions are absorbed by normalizing to the empirical value at a convenient reference energy,

$$J_{\Delta V, E_s}(E) = J_{\Delta V}(E) - J_{\Delta V}(E_s). \quad (15)$$

The energy dependence of the imaginary volume integral is approximated by

$$J_W(E) = J_W^0 [1 - \beta \exp(-\alpha E)]. \quad (16)$$

Our calculation (see Fig. 8) suggests no sharp increase of the real volume integral as the energy falls toward zero, indicating a weak threshold anomaly. It also suggests that optical potentials with $J_V \approx 400 \text{ MeV fm}^3$ would be preferred.

To conclude this section, we find that folding potentials including finite-range, recoil, and density-dependence effects describe well the cross section in the entire angular range, comparable with the more flexible WS form factors. A realistic description of the surface of the nucleon and charge single-particle densities was essential for the procedure. Inclusion of the more elaborate knock-on exchange potential reduces the number of discrete ambiguities, while the dynamical content of the S matrix remains the same, with a strong resonant effect in the low l partial waves.

III. SEMICLASSICAL BARRIER AND INTERNAL BARRIER AMPLITUDES

Once we have established the main features of the average OMP, we turn now to study the reaction mechanism using semiclassical methods. The far-side dominance observed in the angular distributions does not explain the behavior of the S -matrix elements at low angular momentum. The reason is of course that the far/near (F/N) decomposition method does not perform a dynamic decomposition of the scattering function, but merely decomposes the scattering amplitude into traveling waves. The intermediate-angle structures, such as those observed in our angular distribution, have been repeatedly interpreted as arising from the interference of two ranges in angular momenta, $\ell_<$ and $\ell_>$, contributing to the same negative deflection angle. However, the corresponding cross sections, $\sigma_{F<}$ and $\sigma_{F>}$, cannot be isolated because their dynamic content (S matrix) is not accessible.

The semiclassical uniform approximation for the scattering amplitude of Brink and Takigawa [14] is well adapted to describe situations in which the scattering is controlled by at most three active, isolated, complex turning points. An approximate multireflection series expansion of the scattering function can be obtained, the terms of which have the same simple physical meaning as in the exact Debye expansion for

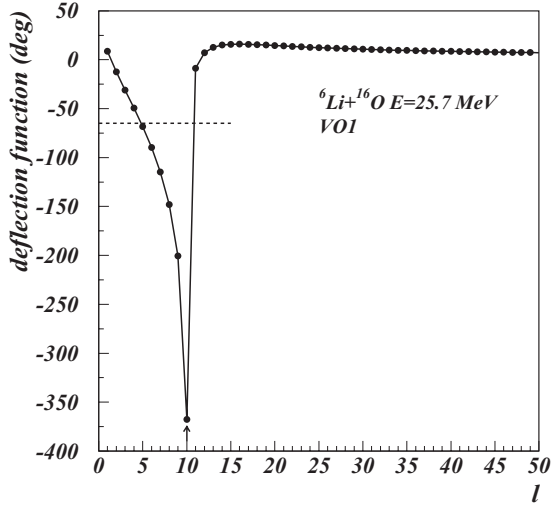


FIG. 9. Semiclassical deflection function using the VO1 parametrization of the bare WS potential. The shape is asymmetric and has a logarithmic singularity at the orbiting momentum $l \approx 10$. The dashed line at $\theta = -65^\circ$ marks the position of the pre-rainbow minimum. The arrow marks the orbiting angular momentum.

the scattering of light on a spherical well. The major interest in this theory comes from the fact that it can give precious information on the response of a nuclear system to the nuclear interior. An application [9] of this technique helped to clarify the controversial problem of the “Airy oscillation” seen in low-energy $^{16}\text{O} + ^{12}\text{C}$ scattering [5].

We take as an example the potential VO1 in Table I. We discard the absorptive term and define the effective potential as

$$V_{\text{eff}}(r) = V(r) + \frac{\hbar^2 \lambda^2}{2\mu r^2}, \quad \lambda = \ell + \frac{1}{2}, \quad (17)$$

where the Langer prescription has been used for the centrifugal term. This guarantees the correct behavior of the semiclassical wave function at the origin [39]. Then we calculate the deflection function

$$\Theta(\lambda) = \pi - 2 \int_{r_1}^{\infty} \frac{\sqrt{\frac{\hbar^2}{2\mu} \lambda^2 dr}}{r^2 \sqrt{E_{\text{c.m.}} - V_{\text{eff}}}}, \quad (18)$$

where r_1 is the outer zero of the square root, i.e., the radius of closest approach to the scatterer, and μ is the reduced mass. Note that with the replacement $\hbar\lambda = b\sqrt{2\mu E}$, Eq. (18) becomes identical to the classical deflection function $\Theta(b)$, where b is the impact parameter. The result is shown in Fig. 9. The behavior of $\Theta(\lambda)$ is the one expected for a strong nuclear potential in a near-orbiting kinematical situation in which the center-of-mass energy approximately equals that of the top of the barrier for some specific angular momentum. All the measured angular range is classically illuminated. The deflection function exhibits no genuine minima, but rather a pronounced cusp close to an orbiting logarithmic singularity. Therefore any interpretation of structures in angular distributions in terms of Airy oscillations can be discarded. Rather, we need an interpretation appropriate for orbiting, a well-

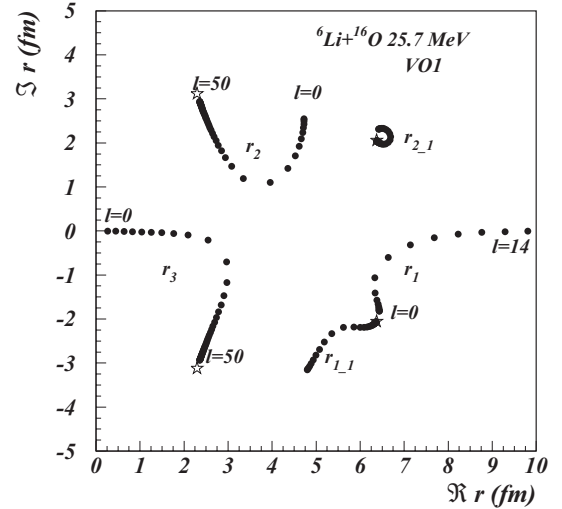


FIG. 10. Trajectories of complex turning points for the potential VO1, Table I. Inactive turning points r_{1-1} and r_{2-1} give negligible small contribution to the semiclassical S matrix and are omitted from the calculation. The complex poles of the potential are plotted with stars.

documented situation in classical physics [40]. We identify the cusp angular momentum as the orbiting momentum (λ_o) since this is related to the coalescence of two (barrier) turning points and the innermost turning point given by the centrifugal barrier becomes classically accessible. There are two branches that can be distinguished, an internal branch for low active momenta $\lambda < \lambda_o$ related to semiclassical trajectories which penetrate into the nuclear pocket and a less-developed external (barrier) branch ($\lambda > \lambda_o$) related to trajectories deflected at the diffuse edge of the potential.

However, this simple calculation cannot reveal the relative importance of these branches and provides no information about the interference effects of the corresponding semiclassical trajectories. To clarify these points it is best to go into the complex r plane and look for complex turning points, i.e., the complex roots of the quantity $E_{\text{c.m.}} - V_{\text{eff}} - iW$. This is an intricate numerical problem, because, for a WS optical potential, the turning points are located near the potential singularities and there are an infinite number of such poles. The situation for integer angular momenta is depicted in Fig. 10. Inactive turning points r_{1-1} and r_{2-1} are located quite far from the real axis and give a negligible small contribution to the total S matrix. We observe an ideal situation with three well-isolated turning points for each partial wave.

The multireflection expansion of the scattering function in the Brink-Takigawa approach reads

$$S_{WKB}(\ell) = \sum_{q=0}^{\infty} S_q(\ell), \quad (19)$$

where

$$S_0(\ell) = \frac{\exp(2i\delta_1^\ell)}{N(S_{21}/\pi)} \quad (20)$$

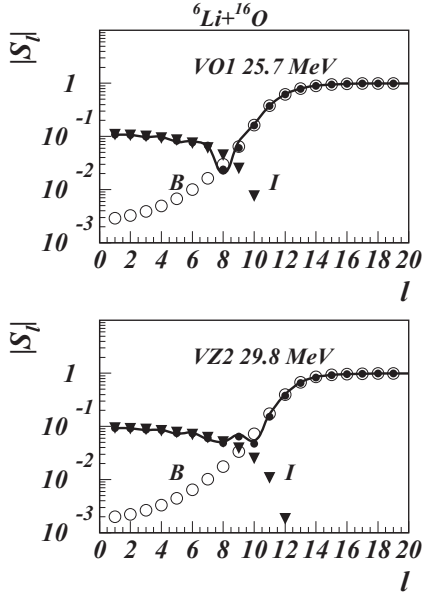


FIG. 11. Semiclassical absorption profile for the WS potentials VO1 and VZ2, Table I. Barrier (open circles) and internal barrier components (triangles) are indicated. The exact total quantum S matrix is indicated by small dots. The line is a cubic spline interpolation of the total semiclassical scattering function for the same potential. The Grünh-Wall dip at $l \sim 8$ appears as interference between barrier and internal barrier amplitudes

and, for $q \neq 0$,

$$S_q(\ell) = (-)^{q+1} \frac{\exp[2i(qS_{32} + S_{21} + \delta_1^\ell)]}{N^{q+1}(S_{21}/\pi)}. \quad (21)$$

In these equations δ_1^ℓ is the WKB (complex) phase shift corresponding to the turning point r_1 , $N(z)$ is the barrier

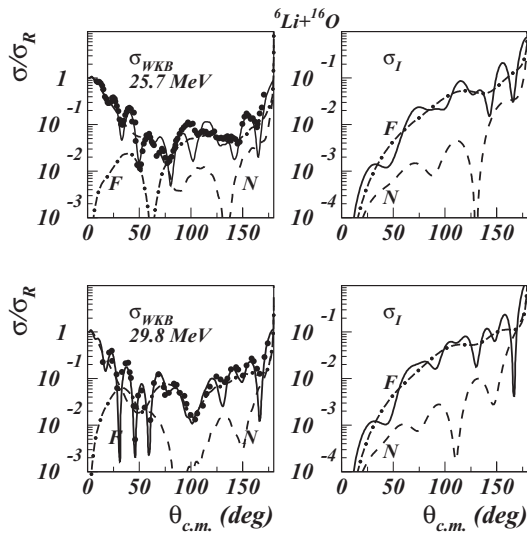


FIG. 12. Semiclassical calculation for ${}^6\text{Li} + {}^{16}\text{O}$ based on potentials VO1 and VZ2 at 25.7 and 29.8 MeV, respectively, Table I. The total cross section (σ_{WKB}) and the internal barrier (σ_I) are further decomposed into far-side (F) and near-side (N) components.

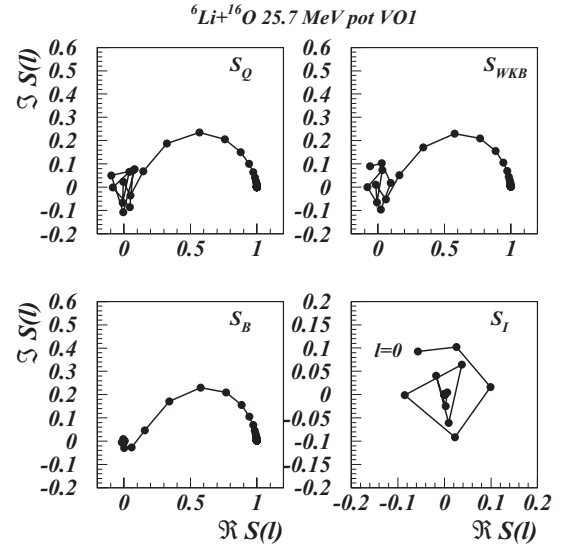


FIG. 13. Argand diagrams for the exact S matrix (S_Q) calculated with WS potential VO1 compared with WKB approximations for the same potential. Barrier S_B and internal-barrier S_I components are shown separately.

penetrability factor,

$$N(z) = \frac{\sqrt{2\pi}}{\Gamma(z + \frac{1}{2})} \exp(z \ln z - z), \quad (22)$$

and S_{ij} is the action integral calculated between turning points r_i and r_j ,

$$S_{ij} = \int_{r_i}^{r_j} dr \left\{ \frac{2\mu}{\hbar^2} [E_{c.m.} - V_{\text{eff}} - iW] \right\}^{1/2}. \quad (23)$$

S_{21} and S_{32} are independent of the integration path provided they lie on the first Riemann sheet and collision with potential poles is avoided. Each term in Eq. (19) has a simple physical

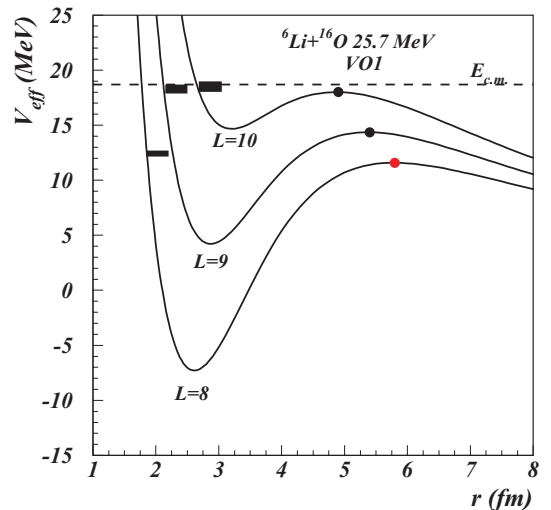


FIG. 14. (Color online) Shape (quasimolecular) resonances (thick lines) in the effective potential based on VO1 parametrization. Only narrow resonances located near the barrier top (dots) are shown for a few active partial waves.

interpretation. The first term (the barrier term, denoted as S_B) retains contributions from trajectories reflected at the barrier, not penetrating the internal region. The q th term corresponds to trajectories refracted q times in the nuclear interior with $q - 1$ reflections at the barrier turning point r_2 . Summation of terms $q \geq 1$ can be recast into a single term,

$$S_l = \frac{\exp[2i(S_{32} + S_{21} + \delta_1^\ell)]}{N(S_{21}/\pi)^2} \frac{1}{1 + \exp[2iS_{32}]/N(S_{21}/\pi)}, \quad (24)$$

and is known as the internal barrier scattering function. The last factor in Eq. (24), the enhancement factor, is responsible for the multiple reflections of the wave within the potential pocket. When the absorption in the nuclear interior is large, the enhancement factor reduces to one, and we are left with the expression used in [21]. Since the semiclassical scattering function is decomposed additively, $S_{WKB} = S_B + S_l$, the corresponding total scattering amplitude is decomposed likewise as $f_{WKB} = f_B + f_l$ and conveniently the corresponding barrier and internal barrier angular distributions are calculated as $\sigma_{B,l} = |f_{B,l}|^2$, using the usual angular momentum expansion of the amplitudes.

The poles of the semiclassical S matrix are given by

$$N(i\epsilon) + e^{2iS_{32}} = 0; \epsilon = -\frac{i}{\pi} S_{21}. \quad (25)$$

This is equivalent to the outgoing boundary condition and can be satisfied only when the energy or the angular momentum is complex and can be used for searching for Regge poles. It should be emphasized that these poles are due to multiple reflections of the internal wave within the potential pocket, while the zeros of the S matrix arise from the interference

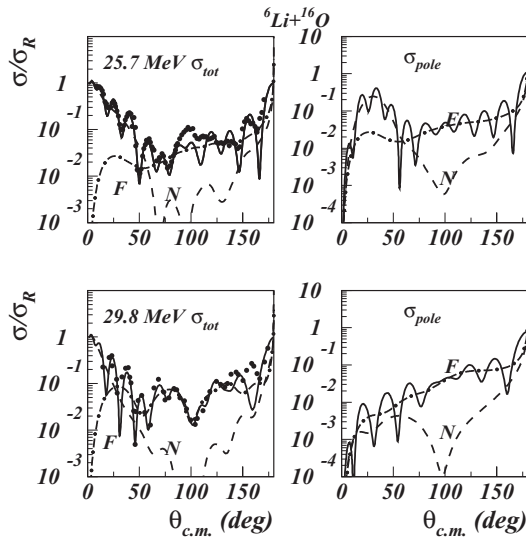


FIG. 15. Comparison of the data with a Regge pole calculation using the parametrization given in Table II (left panels, σ_{tot}). The pole σ_{pole} components are shown in the right panels. Each component is further decomposed into far-side (F) and near-side (N) components. The shallow minimum in the far-side component of the total cross section appears as interference between background and pole components.

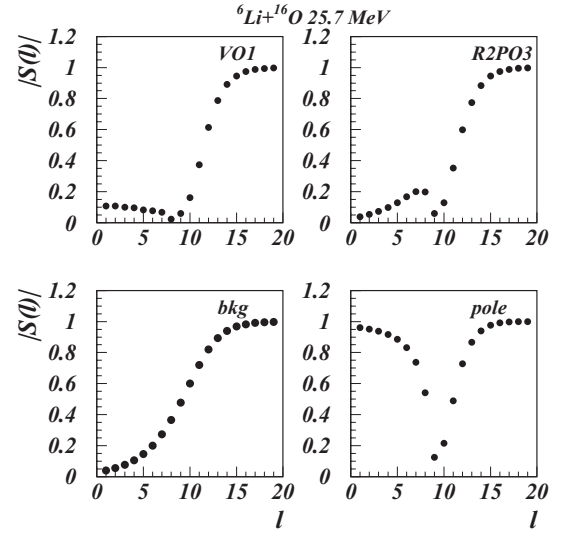


FIG. 16. Absorption profile for the WS potential VO1 compared with the results for the two-pole calculation. The Grün-Wall dip at $l \sim 9$ is due to the pole component in the S matrix.

between the barrier and internal barrier waves. The accuracy of the semiclassical calculation has been checked by comparing the barrier and internal barrier absorption profiles with the exact quantum-mechanical result in Fig. 11. First, one observes that the semiclassical B/I expansion is an exact decomposition of the quantum result. They are virtually identical at the scale of the figure. The internal component gets significant values up to the grazing angular momentum ($\ell_g = 12$) and is negligibly small beyond this value. The barrier component resembles a strong absorption profile and this justifies the interpretation that it corresponds to that part of the flux not penetrating into the nuclear interior. For values near the orbiting angular momentum ($\ell_o \approx 10$), the two components interfere and a downward spike appears in the total profile, in complete

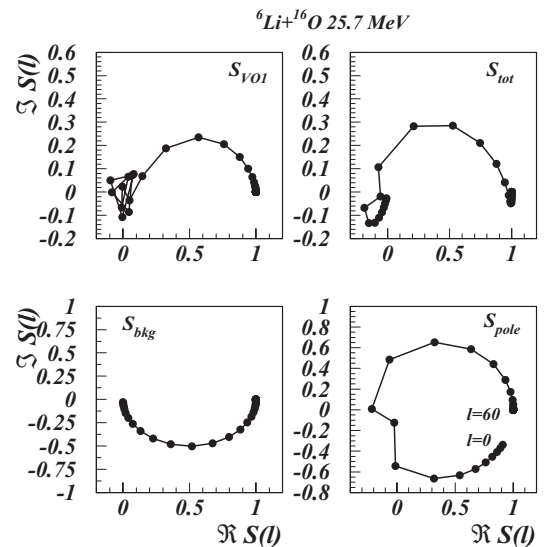


FIG. 17. Argand diagrams for the S matrix calculated with WS potential VO1 compared with the two-Regge-pole approximation (Table II).

TABLE II. Parameters for two-Regge-pole unitary solutions for ${}^6\text{Li} + {}^{16}\text{O}$. The first four columns define the background S matrix and the next ones define the pole component. The approximate pole and zero positions predicted by the model in the complex l plane are given by $L_i + ip_i$ and $L_i + iz_i$, respectively. See text for notation.

E_{lab}	L	Δ	α	β	L_1	Δ_1	D_1	Γ_1	L_2	Δ_2	D_2	Γ_2	χ^2	σ_R
25.7	14.73	3.08	-1.57	0.29	9.82	1.72	3.10	5.03	8.97	1.02	0.41	1.19	4.32	1437
29.8	10.07	1.53	1.59	5.09	4.71	4.42	2.27	1.13	6.37	0.65	4.38	0.97	11.8	1117

agreement with the quantum result. This is the famous Grünh-Wall spike [41] introduced phenomenologically to explain ALAS for α -particle scattering and appears here as strong interference between barrier and internal barrier amplitudes. Second, the B/I components are almost decoupled in the angular momentum space and therefore they will contribute in different angular ranges.

Semiclassical cross sections are compared with the data in Fig. 12. Better insight into this technique is obtained by further decomposing the B/I components into far and near (BF/BN and IF/IN) subcomponents. Clearly, the barrier component dominates the forward angle region. Fraunhofer diffractive oscillations appear as the result of BF and BN interference. At large angles, the internal contribution accounts for the full cross section.

Thus, the intermediate-angle exotic structure in angular distributions for the elastic scattering of ${}^6\text{Li}$ on ${}^{16}\text{O}$ can be understood as a result of coherent interference of two far-side subamplitudes generated by different terms in the uniform multireflection expansion of the scattering function [terms $q = 0$ and $q = 1$ in Eq. (19)], corresponding to the scattering at the barrier and the internal barrier. This interference effect appears as a signature of a surprisingly transparent interaction potential for the loosely bound nucleus ${}^6\text{Li}$ at this low energy, which allows part of the incident flux to penetrate the nuclear interior and re-emerge with significant probability.

The Argand diagrams corresponding to the B/I decomposition are displayed in Fig. 13. Evidently, only the internal barrier amplitude is responsible for the resonant behavior of the low-momentum partial waves.

IV. REGGE POLES

We have seen in the preceding sections that the data could be described by highly transparent potentials, such that the low absorption is not able to suppress the resonant effects in the low partial waves. Semiclassically, these effects appear as a consequence of multiple reflections of the internal amplitude between the most internal complex turning points of the potential. In fact, a common property of the WS potentials which well describe the data is that they possess several narrow shape (molecular) resonances located in the most active waves $l = 8, 9, 10$ (see Fig. 14). In this section we examine this effect in terms of a purely phenomenological Regge pole approximation. Previously, Ceuleneer and Michel [42] used the Cowley and Heymann [43] expansion of the scattering amplitude to describe $\alpha + {}^{16}\text{O}$ scattering at low energy. We adopt the ‘‘product’’ representation of the S matrix [15],

$$S(l) = S_{bkg}(l)S_{\text{pole}}(l), \quad (26)$$

where the background (bkg) component is borrowed from the strong absorption model of Ericson [44],

$$S_{bkg} = \left[1 + \beta \exp(-i\alpha) \exp\left(\frac{L-l}{\Delta}\right) \right]^{-1}. \quad (27)$$

For the pole term we adopt the expression

$$S_{\text{pole}}(l) = \prod_{i=1}^2 \left[1 + i \frac{D_i(l)}{l - L_i - i\hat{\Gamma}_i(l)/2} \right]. \quad (28)$$

This term describes resonances in l centered at L_i with total width $\hat{\Gamma}_i$. In line with McVoy [15] we assume the zeros and the widths to be slowly l dependent and vanishingly small as $l \rightarrow \infty$,

$$D_i(l) = \frac{D_i}{1 + \exp\left(\frac{l-L}{\Delta_i}\right)}, \quad (29)$$

$$\hat{\Gamma}_i(l) = \frac{\Gamma_i}{1 + \exp\left(\frac{l-L}{\Delta_i}\right)}. \quad (30)$$

Clearly, D measures the distance between the pole ($p = 1/2\Gamma$) and the zero ($z = 1/2\Gamma - D$). The model has 12 parameters, twice as much as the WS model. The reason is that we were not able to find a single-pole unitary solution for both background and pole components. Since the problem is highly nonlinear there is no guarantee for the uniqueness of the solution. We used a Monte Carlo procedure to generate input parameters and then minimized the usual χ^2 objective function. From the numerous solutions we found, we choose to show only one set of parameters (Table II) which has the merit that both S_{bkg} and S_{pole} are unitary. The poles are located in the upper complex l near $L \approx 9, 10$, in line with what we found from the other analyses. The cross sections obtained with this model are plotted in Fig. 15. The background component is important only at forward angles, while the pole component contributes significantly at all angles. Only the pole component contributes to the far-side amplitude, which displays only a shallow minimum near $\theta = 50^\circ$. The nearby deep minimum, interpreted previously as a Fraunhofer minimum, appears here as a result of the strong destructive interference between far- and near-side amplitudes of the pole component alone. The background absorption profile shown in Fig. 16 is typical for the strong absorption regime while the Grünh-Wall dip appears here, as carried out by the pole component alone. The corresponding Argand diagrams displayed in Fig. 17 show clearly the resonant contribution of the pole component.

V. CONCLUSIONS

We have analyzed ${}^6\text{Li} + {}^{16}\text{O}$ elastic scattering at an energy of 4–5 MeV/nucleon in an effort to obtain systematic information on the interaction of p -shell nuclei with light targets. Optical potentials for these nuclei are needed for studies where highly peripheral transfer reactions involving radioactive nuclei are used as indirect methods for nuclear astrophysics and are an important factor in the accuracy and reliability of these methods. At the present time, the best information on the optical potentials for radioactive nuclei can be obtained only by extrapolation from adjacent less-exotic nuclei. Our intention is to narrow the ambiguities in the optical model potentials by systematic studies of the scattering of loosely bound projectiles over a large range of angles and energies and to extract information that can be used for systems involving radioactive projectiles, for which elastic scattering data of very good quality are not easily available.

The data confirm the existence of an exotic intermediate-angle structure, observed previously [4] at higher energy. We interpret these structures as refractive effects arising from a fine balance between the real and imaginary components of the optical potential. We have performed a traditional analysis of the data in terms of Woods-Saxon and microscopic folded potentials. A range of effective NN interactions has been used to generate folding potentials. Both approaches lead to the conclusion that the optical potential is deep and surprisingly transparent, in line with findings for other more bound systems. Folding model form factors have been renormalized in the usual way in order to account for the energy and radial dependence of the dynamic polarization potential. The intermediate-angle structures could be reproduced only with potentials approaching a critical volume integral of about 280 ± 10 MeV fm³ and a rms radius $R_V = 4.05 \pm 0.1$ fm and, consequently, are severely selective, limiting the ambiguities in the determination of the OMP. The remaining discrete ambiguities could be removed by including an exact local representation of the knock-on exchange kernel within a Perey-Saxon localization procedure. Our analysis in terms of the dispersion relation confirms the conjecture of a canceling effect between the repulsive dynamic polarization potential due to the coupling with breakup channels and the attractive, dispersive component of the optical potential. Thus the barrier anomaly appears to be weak in this case. As a consequence, all folding potentials require a renormalization $N_V < 1$ to match the required critical value of the real volume integral.

The present analysis shows that in order to reproduce the structures observed at intermediate angles in this case, one needs to allow for a more complicated radial dependence of the dynamic polarization potential, which can be energy and target dependent, and requires deep real potentials.

In an effort to clarify the reaction mechanism responsible for the intermediate-angle structures, we performed extensive semiclassical calculations within the uniform multireflection expansion of the scattering function of Brink and Takigawa. It has been shown that using complex trajectories, the (external) barrier/internal barrier expansion is an exact realization of the dynamic decomposition of the quantum result into components responsible for that part of the incident flux reflected at the barrier and the part of the flux which penetrates into the nuclear interior and re-emerges with significant probability. By combining the B/I decomposition with the usual far-side/near-side expansion, we explain the intermediate-angle structure as a coherent interference effect of two subamplitudes (BF and IF). Intermediate-angle structures in our case do not arise from interference between two saddle points in the same term of the multireflection expansion but from interference between a saddle point from the second term of the expansion, describing trajectories refracted in the internal region, and a contribution from the first term of the expansion [see Eqs. (19)–(21)]. Thus, this refractive effect appears as a signature of a highly transparent interaction potential. This decomposition allows us to isolate dynamically the resonant component of the S matrix which is due to multiple reflections of the low-angular-momentum waves between the most internal complex turning points of the potential.

A completely different picture emerges by using a slight generalization of the “product” Regge representation of the full S matrix in which poles in the complex l plane are located in peripheral waves. Seeking a unitary solution, we found that the pole component is entirely responsible for intermediate-angle structure and the oscillatory behavior of the cross section at large angles. Thus it is a matter of taste whether we interpret intermediate-angle structure as a resonant refraction or equally well as a resonant diffraction.

ACKNOWLEDGMENTS

This work was supported in part by UEFISCDI-Romania under program PN-II Contract No. 55/05.10.2011 and by the US Department of Energy under Grant No. DE-FG02-93ER40773. We are grateful to Dr. M. F. Vineyard for sending us tabular data.

-
- [1] G. R. Satchler and W. G. Love, *Phys. Rep.* **55**, 183 (1979).
 - [2] M. E. Brandan and G. R. Satchler, *Phys. Rep.* **285**, 143 (1997).
 - [3] L. Trache, A. Azhari, H. L. Clark, C. A. Gagliardi, Y.-W. Lui, A. M. Mukhamedzhanov, R. E. Tribble, and F. Carstoiu, *Phys. Rev. C* **61**, 024612 (2000).
 - [4] F. Carstoiu, L. Trache, R. E. Tribble, and C. A. Gagliardi, *Phys. Rev. C* **70**, 054610 (2004).
 - [5] A. A. Ogloblin *et al.*, *Phys. Rev. C* **62**, 044601 (2000).
 - [6] S. Szilner *et al.*, *Phys. Rev. C* **64**, 064614 (2001).
 - [7] E. Stiliaris *et al.*, *Phys. Lett. B* **223**, 291 (1989).
 - [8] J. Knoll and R. Schaeffer, *Ann. Phys. (NY)* **97**, 307 (1976).
 - [9] R. Anni, *Phys. Rev. C* **63**, 031601(R) (2001).
 - [10] H. Feshbach, *Ann. Phys. (NY)* **5**, 357 (1958); **19**, 287 (1962).
 - [11] Y. Sakuragi, *Phys. Rev. C* **35**, 2161 (1987).
 - [12] C. Mahaux, H. Ngo, and G. R. Satchler, *Nucl. Phys. A* **449**, 354 (1986).
 - [13] J. P. Jeukenne, A. Lejeune, and C. Mahaux, *Phys. Rev. C* **16**, 80 (1977).

- [14] D. M. Brink and N. Takigawa, *Nucl. Phys. A* **279**, 159 (1977).
- [15] K. W. McVoy, *Phys. Rev. C* **3**, 1104 (1971).
- [16] M. F. Vineyard, J. Cook, K. W. Kemper, and M. N. Stephens, *Phys. Rev. C* **30**, 916 (1984), and private communication.
- [17] V. I. Chuev, V. V. Davidov, B. G. Novatskii, A. A. Oglobin, S. B. Sakuta, and D. N. Stepanov, *J. Phys. (Paris) Suppl. C* **6**, 161 (1971).
- [18] F. Michel, S. Ohkubo, and G. Reidemeister, *Prog. Theor. Phys. Suppl.* **132**, 7 (1998).
- [19] M. S. Hussein and K. W. McVoy, *Nucl. Phys. A* **445**, 123 (1985).
- [20] A. Bonaccorso and F. Carstoiu, *Nucl. Phys. A* **706**, 322 (2002).
- [21] F. Michel, G. Reidemeister, and S. Ohkubo, *Phys. Rev. Lett.* **89**, 152701 (2002); *Phys. Rev. C* **63**, 034620 (2001).
- [22] R. M. Drisko, G. R. Satchler, and R. H. Bassel, *Phys. Lett.* **5**, 347 (1963).
- [23] N. Anantaraman, H. Toki, and G. F. Bertsch, *Nucl. Phys. A* **398**, 269 (1983).
- [24] M. Beiner and R. J. Lombard, *Ann. Phys. (NY)* **86**, 262 (1974).
- [25] I. Angeli, *Heavy Ion Phys.* **8**, 23 (1998).
- [26] D. T. Khoa, G. R. Satchler, and W. von Oertzen, *Phys. Rev. C* **61**, 954 (1997).
- [27] J. W. Negele and K. Yazaki, *Phys. Rev. Lett.* **47**, 71 (1981).
- [28] S. Misticu and F. Carstoiu, *Phys. Rev. C* **83**, 054622 (2011).
- [29] D. Gogny, in *Proceedings of the International Conference on Nuclear Physics, Munich 1973*, edited by J. de Boer and H. J. Mang (North Holland Publ. Co, Amsterdam, 1973), Vol. 1, p. 48.
- [30] D. H. Youngblood, H. L. Clark, and Y.-W. Lui, *Phys. Rev. Lett.* **82**, 691 (1999).
- [31] G. Colo, N. Van Giai, P. F. Bortignon, and M. R. Quaglia, *Phys. Lett. B* **485**, 362 (2000).
- [32] M. A. Nagarajan, C. C. Mahaux, and G. R. Satchler, *Phys. Rev. Lett.* **54**, 1136 (1985).
- [33] S. Kailas, *Phys. Rev. C* **41**, 2943 (1990).
- [34] M. A. Tiede, D. E. Trcka, and K. W. Kemper, *Phys. Rev. C* **44**, 1698 (1991).
- [35] N. Keeley, S. J. Bennett, N. M. Clarke, B. R. Fulton, G. Tungate, P. V. Drumm, M. A. Nagarajan, and J. S. Lilley, *Nucl. Phys. A* **571**, 326 (1994).
- [36] C. Beck *et al.*, *Phys. Rev. C* **67**, 054602 (2003).
- [37] D. H. Luong *et al.*, *EPJ Web Conf.* **17**, 03002 (2011).
- [38] D. E. Trcka, A. D. Frawley, K. W. Kemper, D. Robson, J. D. Fox, and E. G. Myers, *Phys. Rev. C* **41**, 2134 (1990).
- [39] P. Fröbrich and R. Lipperheide, *Theory of Nuclear Reactions* (Clarendon, Oxford, 1996).
- [40] K. W. Ford and J. A. Wheeler, *Ann. Phys. (NY)* **7**, 259 (1959).
- [41] C. R. Grünh and N. S. Wall, *Nucl. Phys. A* **81**, 161 (1966).
- [42] R. Ceuleneer and F. Michel, *Phys. Lett.* **43B**, 365 (1973).
- [43] A. A. Cowley and C. Heymann, *Nucl. Phys. A* **146**, 465 (1970).
- [44] T. E. O. Ericson, *Preludes in Theoretical Physics*, edited by A. de-Shalit, L. Van Hove, and H. Feshbach (North Holland, Amsterdam, 1965).